University Library

MINERVA ACCESS

A gateway to Melbourne's research publications

Minerva Access is the Institutional Repository of The University of Melbourne

Author/s:
Acharya, R;Coke, M;Adshead, M;Li, K;Achinuq, B;Cai, R;Gholizadeh, AB;Jacobs, J;Boland, JL;Haigh, SJ;Moore, KL;Jamieson, DN;Curry, RJ

Title:
Highly 28Si enriched silicon by localised focused ion beam implantation

Date:
2024-12-01

Citation:
Acharya, R., Coke, M., Adshead, M., Li, K., Achinuq, B., Cai, R., Gholizadeh, A. B., Jacobs, J., Boland, J. L., Haigh, S. J., Moore, K. L., Jamieson, D. N. & Curry, R. J. (2024). Highly 28Si enriched silicon by localised focused ion beam implantation. Communications Materials, 5 (1), https://doi.org/10.1038/s43246-024-00498-0.

Persistent Link:
https://hdl.handle.net/11343/352725

License:
cc-by

communications materials

Article

https://doi.org/10.1038/s43246-024-00498-0

Highly ^{28}Si enriched silicon by localised focused ion beam implantation

Check for updates

Ravi Acharya [1,2] ✉, Maddison Coke[1], Mason Adshead[1], Kexue Li[3], Barat Achinuq[4], Rongsheng Cai[4], A. Baset Gholizadeh[1,5], Janet Jacobs [1], Jessica L. Boland [1], Sarah J. Haigh [4], Katie L. Moore [3], David N. Jamieson [2] & Richard J. Curry [1] ✉

Solid-state spin qubits within silicon crystals at mK temperatures show great promise in the realisation of a fully scalable quantum computation platform. Qubit coherence times are limited in natural silicon owing to coupling to the ^{29}Si isotope which has a non-zero nuclear spin. This work presents a method for the depletion of ^{29}Si in localised volumes of natural silicon wafers by irradiation using a 45 keV ^{28}Si focused ion beam with fluences above 1×10^{19} ions cm^{-2}. Nanoscale secondary ion mass spectrometry analysis of the irradiated volumes shows residual ^{29}Si concentration down to 2.3 ± 0.7 ppm and with residual C and O comparable to the background concentration in the unimplanted wafer. After annealing, transmission electron microscopy lattice images confirm the solid phase epitaxial re-crystallization of the as-implanted amorphous enriched volume extending over 200 nm in depth.

Development of device architectures for a large-scale quantum computer are underway worldwide[1]. A crucial issue for all these approaches is the need to develop robust qubits that allow high-fidelity operation. Coherent quantum systems are highly sensitive to their local environment which leads to qubit decoherence. This necessitates the use of quantum error correction codes[2] which impose significant engineering overheads such that millions of qubits are required to realise a fault-tolerant quantum computer[3].

Spin qubits in silicon present a promising platform to realise scalable quantum computation[4] due to their long coherence times in the solid-state and high gate fidelities[5–7], as well as being able to borrow techniques from the materials and processes employed for industrial nano-fabrication[8]. However, in natural silicon (^{Nat}Si), the nuclear spin $I = 1/2$ ^{29}Si isotope with abundance 4.68%[10] acts to limit electron spin qubit coherence times in donor and dot architectures. This is due to the dipole-induced ^{29}Si nuclear spin flip-flops within the ^{29}Si nuclear spin bath surrounding the electron spin[11–13]. In isotopically enriched ^{28}Si ($I = 0$), electron spin qubit coherence times can be significantly increased. For example, a substrate with 800 ppm residual ^{29}Si has led to a factor of 5000 improvement in the electron pure dephasing time (T^*_{2e}) as compared to ^{Nat}Si[6]. The enrichment method presented here depletes both ^{29}Si and ^{30}Si to provide a matrix composed predominantly of a single isotope. This therefore reduces lattice strain caused by isotopic mass variations in the crystal lattice that can perturb the hyperfine interaction between the donor nucleus and electron[14]. The method also minimises the background concentration of impurities and lattice defects that may couple to the qubit.

Several previous techniques have been applied to produce enriched ^{28}Si (Table 1). The highest quality material regarding both enrichment and contamination was produced for the Avogadro project[15], where centrifugation was employed to produce $^{28}SiF_4$. The combined background ^{30}Si and ^{29}Si isotopic level of ~50 ppm was later improved upon by the kg-2 project[16] which reported residual ^{29}Si and ^{30}Si levels of 6.6 ppm and 0.38 ppm, respectively. Ion beams that employ mass-filtering using magnetic and electric fields have also been used to create isotopically enriched material. An example of this procedure is the creation of epitaxial enriched thin films via hyperthermal ion beam deposition employing a Penning ion source[17–19] from a natural silane source gas. However, the material is reported to contain a significant level of C and O, greater than the backgrounds found in device grade silicon wafers. Our present method builds on the work by Holmes et al.[20] that employed high fluence irradiation by a 45 keV $^{28}Si^-$ broad ion beam to demonstrate depletion of ^{29}Si to a level of 250 ppm over areas of ~1×1 cm^2. The negative ion beam suppressed isobar contamination (N_2 and CO) of the beam typically present in positive ion implanter systems.

Our method enriches localised volumes by employing a focused ^{28}Si ion beam (Fig. 1a). The focused beam provides a higher beam current intensity leading to relatively short irradiation times that would otherwise be

[1]Department of Electrical and Electronic Engineering, Photon Science Institute, University of Manchester, Manchester M13 9PL, UK. [2]School of Physics, University of Melbourne, Parkville, Melbourne, VIC 3010, Australia. [3]Department of Materials, Photon Science Institute, University of Manchester, Manchester M13 9PL, UK. [4]Department of Materials, University of Manchester, Manchester M13 9PL, UK. [5]Present address: Microsoft, Romsey, UK.
✉e-mail: ravi.acharya@student.manchester.ac.uk; richard.curry@manchester.ac.uk

Table 1 | A summary of the reported ^{29}Si and ^{30}Si depletion levels, and background contaminant levels, reached by a variety of different enrichment techniques

Reference	Isotopic selection/growth method	^{29}Si (ppm)	^{30}Si (ppm)	C (cm^{-3})	O (cm^{-3})
Avogadro project[15]	Centrifuge/CVD	<50.65	<50.65	$(3.4 \pm 4.0) \times 10^{14}$	$(2.1 \pm 1) \times 10^{14}$
kg-2 project[16]	Centrifuge/CVD	6.583 ± 0.031	0.378 ± 0.010	$<4 \times 10^{15}$	$<5 \times 10^{14}$
Mazzocchi et al.[32]	Centrifuge/CVD	52.4 ± 9.0	13.9 ± 5.0		
Sabbagh et al.[33]	Centrifuge/CVD	800	10	$<4 \times 10^{17}$	$<1 \times 10^{18}$
Li et al.[34]	Centrifuge/CVD	800	20		
Holmes et al.[20]	Magnetic separation/^{28}Si^{-} broad beam implant	250	160	1×10^{17}	3×10^{17}
Tang et al.[18]	Magnetic separation/Ion beam deposition	0.832	0.490	9.5×10^{18}	2.1×10^{18}
This work—sample 1	Wien filter/^{28}Si^{++} focused beam implant	12.0 ± 2.3	6.0 ± 1.7		
This work—sample 2	Wien filter/^{28}Si^{++} focused beam implant	2.3 ± 0.7	0.6 ± 0.4		
This work—sample 3	Wien filter/^{28}Si^{++} focused beam implant	6.1 ± 0.9	2.4 ± 0.6	$<2.5 \times 10^{15}$	$<2.5 \times 10^{15}$

For each reference both the isotopic selection and growth method are stated (CVD is chemical vapour deposition). The results outlined in this work employing the use of a focused ion beam are also shown. Each value is quoted to the same precision that was reported.

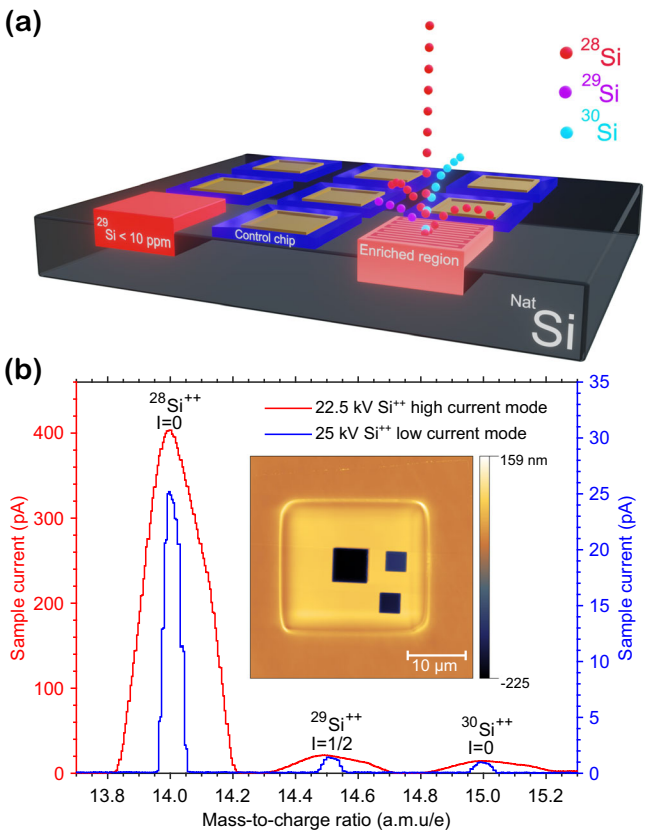

Fig. 1 | Focused ion beam isotopic enrichment using the P-NAME tool. **a** Schematic depicting the isotopic enrichment of localised volumes using a focused ion beam composed of ^{28}Si where compatible qubit control and interconnect electronics are shown to be integrated following the architecture of ref. 21. **b** Si^{++} Wien filter scans highlighting the isotopic mass resolution of the P-NAME tool. The red high-current scan is taken at an anode voltage of 22.5 kV whereas the blue low-current scan is taken using an anode voltage of 25 kV. The inset of the plot shows the AFM surface map of the as-implanted enriched volume of sample 1 taken after SIMS analysis. The lighter raised square is the implanted area while the dark squares are areas where SIMS has been performed.

impractical on a broad beam ion implanter. We show that this approach results in a residual ^{29}Si and ^{30}Si level that can exceed the kg-2 project but employs standard natural silicon source materials in one machine. Although the focused ion beam source produces positive ions, the proportion of isobars is negligible compared to a broad beam implanter. Also, the vacuum system has orders of magnitude lower vacuum base pressure that, as shown here, led to minimal contamination of the enriched volume.

Our motivation for localised enrichment is that for prototype silicon based quantum computer devices employing donor spins, it is only necessary to enrich the localised volume that houses the qubits[21]. A near-term application of our technique would be to fabricate an improved single-donor qubit device exploiting a localised highly enriched volume. Previous work reported a single ^{31}P donor flip-flop qubit device[22] constructed in an epitaxial enriched ^{28}Si epilayer in which the ^{29}Si concentration had been depleted to 730 ppm. At this level of depletion, ~10 ^{29}Si atoms could be located within the Bohr radius of the ^{31}P donor[23], some of which may perturb the qubit. For example, by use of NMR RF pulses tuned to the ^{29}Si nuclear transitions, the signal from at least three ^{29}Si nuclei was observed by their effect on the flip-flop qubit[22]. The most highly depleted material reported in the present work, with 2.3 ppm ^{29}Si, has on average only 0.004 ^{29}Si atoms within the Bohr radius of each phosphorous donor qubit. This would greatly suppress perturbations from ^{29}Si in a large-scale donor qubit device, where it would also be possible to direct-write depleted vias for qubit coupling.

Results and discussion

Focused ion beam enrichment

Enrichment was performed with a ^{28}Si ion beam provided by the platform for nanoscale advanced materials engineering (P-NAME) tool[24] developed by Ionoptika Ltd. The P-NAME tool is a focused ion beam (FIB) system that incorporates a liquid metal alloy ion source (LMAIS) from which an ion beam is extracted by field ionisation from a sharp emitter tip and subsequently accelerated to keV energies. The P-NAME ion column and sample chamber are held at base pressures of 10^{-8} mbar and 10^{-9} mbar, respectively, thus minimising contamination of the sample from residual gas. An $\mathbf{E} \times \mathbf{B}$ Wien filter is employed to separate isotopes emitted from the source. Ion optical elements in the column provide beam focusing and scanning, filtration of neutral ions and beam collimation apertures. The sample is placed on a stage angled at 3° with respect to the beam in order to minimise ion channelling. By recording the beam current on the sample stage with a Faraday cup as a function of the applied potential in the Wien filter, it is possible to record and select a specific ion mass from the source as shown in Fig. 1b. The mass resolution of the Wien filter, defined as $M/\Delta M$ for the Si^{++} isotopes, is on average 55 ± 12 under high-current mode operation, where a 300 µm resolving aperture is in place along the ion column. Here the resolution for each isotope is obtained from the Gaussian fitting parameters of the respective Wien filter scan peak.

In this work, a series of samples were produced with localised enriched volumes implanted with ^{28}Si^{++} fluences within the range

$0.84 \times 10^{19} - 1.18 \times 10^{19}$ ions cm^{-2}. All other sample-specific parameters are provided in Table 2. The LMAISs used were either AuSiSb or AuSiEr eutectic alloys. The field ionisation process in a LMAIS does not contribute measurable isobar contamination to the ion beam. An accelerating anode potential of 22.5 kV along with the doubly charged $^{28}Si^{++}$ ions meant that the kinetic energy of the beam was 45 keV. This beam energy was predicted to produce a near-planar implanted volume, as TRIDYN[25,26] modelling has previously shown a sputtering yield of near one at this energy [20]. For this work, an ion beam current of the order of 350 pA was focused into a typical beam diameter of ~500 nm which was raster scanned over a 22 μm × 22 μm implantation area. For the flip-flop donor qubit architecture with an inter-qubit spacing of 200 nm, this implanted area could house a 12,000 flip-flop qubit array [27]. The ion beam current was measured in a secondary-electron-suppressed Faraday cup adjacent to the sample before and after the sample irradiation, and the incident beam current was inferred from the average of these two measurements, which typically agreed to a precision of better than 4%. The beam stability during irradiation was monitored by recording the current from an upstream collimator. The chamber is also equipped with a scanning electron microscope that is used to identify specific locations for ion irradiation with respect to pre-fabricated location markers located away from the enriched areas. Following implantation, a two-step annealing recipe was used to regrow the amorphous volume resulting from the implantation. The first annealing step of 620 °C for 10 min was followed immediately by a second step of 1000 °C for 5 s[20].

Table 2 | A summary of the implantation and annealing parameters used for the fabrication of the isotopically enriched ^{28}Si samples outlined in this work

Sample	$^{28}Si^{++}$ ion fluence [×10^{19} ions cm^{-2}]	Ion beam current [pA]	Ion beam width [nm]	Annealed
1	(0.84 ± 0.01)	361 ± 3	730 ± 60	No
2	(1.18 ± 0.04)	380 ± 14	730 ± 60	No
3	(1.13 ± 0.01)	340 ± 8	400 ± 60/ 230 ± 30	Yes
4	(1.08 ± 0.01)	330 ± 2	480 ± 6/ 310 ± 30	No
5	(0.84 ± 0.08)	330 ± 2 (~53 %) + 159 ± 2 (~47 %)	320 ± 70	Yes

Each sample was composed of a single localised 22 μm × 22 μm square enriched area and enriched using a $^{28}Si^{++}$ focused ion beam accelerated under a potential of 22.5 kV to yield a kinetic energy of 45 keV. Samples 3 and 5 were annealed under an ambient Ar atmosphere using a two-step process consisting of an initial step of 620 °C for 10 min followed by a second step of 1000 °C for 5 s. In instances where significant ion beam astigmatism was present two ion beam width values measured along orthogonal axes are quoted in order to quantify the extent of the beam astigmatism.

Enrichment measurement

In order to quantify the enrichment and residual contamination levels within the implanted regions, nanoscale secondary ion mass spectrometry (NanoSIMS) analysis was performed on samples 1, 2, and 3 using a Cs^+ beam to sputter the sample. Depth profiles of the measured isotopic ratios for each of the three silicon isotopes, normalised by dividing each by the sum of the three silicon isotope count values ($Si_T = {}^{28}Si + {}^{29}Si + {}^{30}Si$), are shown for the two as-implanted samples 1 and 2 in Fig. 2. The initial SIMS signal (shown within the shaded grey areas of each profile in Fig. 2) is influenced by the expected steady-state artefact whereby a threshold dose of Cs^+ has to be implanted before both the Cs^+ implantation and sample sputtering rate reach a dynamic equilibrium[28] and can therefore be excluded from the true profiles. At the high ^{28}Si fluences employed here the variation in the Si isotopic ratio profiles of all samples indicates that atom mixing occurs throughout the depth of the enriched volume by a combination of mechanisms including deposition, surface sputtering and forward recoils.

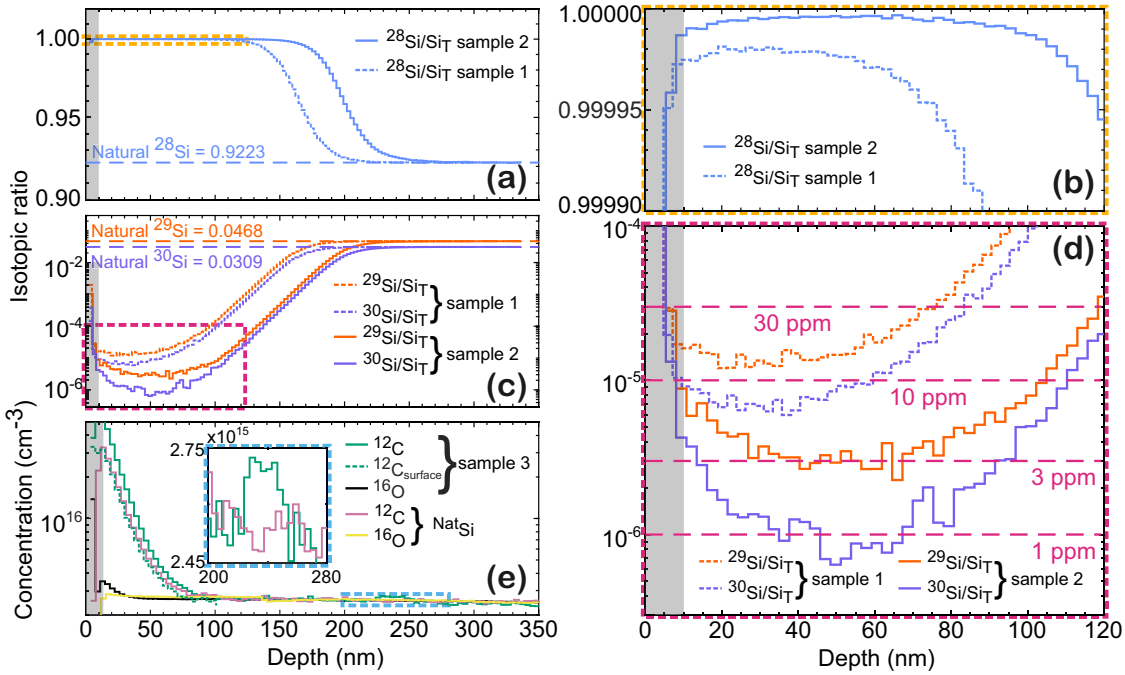

Fig. 2 | NanoSIMS isotopic elemental analysis on isotopically enriched samples. **a**–**d** show depth profiles of the measured isotopic ratios for each of the three silicon isotopes from samples 1 (dotted line) and 2 (solid line), which have been normalised by dividing each by $Si_T = {}^{28}Si + {}^{29}Si + {}^{30}Si$. **b** and **d** are enlarged from the dotted regions outlined within (**a**) and (**c**), respectively. **e** shows the ^{12}C and ^{16}O concentration depth profiles for sample 3 which was annealed following enrichment. The near-surface carbon signal shown by the dotted green line in part (**e**) was selected such that surface contaminants introduced during sample transfer were excluded (see Supplementary Fig. 5). This near-surface signal along with the oxygen profile shows the limited introduction of impurities within the enriched region relative to the unimplanted substrate. The figure inset to (**e**) illustrates ^{12}C gettering observed near the bottom of the enriched volume where the C concentration rises above the minimum detectable limit. The concentration at each depth is the average value across the 5 μm by 5 μm area sampled within each of the enriched volumes during the SIMS analysis. The shaded grey box in each plot indicates the portion of the SIMS depth profile affected by the steady-state artefact and thus excluded from the analysis.

Atomic force microscopy (AFM) measurements on as-implanted samples for fluences above ~1×10^{18} ions cm^{-2} show a consistent increase in the volume of the implanted area that scales with the implanted ion fluence (see Supplementary Fig. 1). This effect is not accounted for in TRIDYN simulations which predict a sputtering yield of one (for further TRIDYN analysis of the amorphous implanted layer see Supplementary Fig. 2). We note that the experimental deviation from the simulations for this higher fluence regime likely arise from ion interactions not accounted for in the modelling. An AFM surface map of sample 1 post-SIMS analysis, inset to Fig. 1b, shows the presence of both this increased volume that is apparent from surface swelling as well as a prominent ridge around the boundary of the implanted area. UV Raman spectra shown in Supplementary Fig. 3, taken from this boundary ridge on an as-implanted sample identify this as being composed of sp^2 amorphous carbon. Further Raman spectra show the absence of carbon from both the unimplanted surrounding substrate and within the implanted area. We assume the observed accumulation of superficial sp^2 amorphous carbon around the boundary of the irradiated area arises from ion beam-induced dissociation of a hydrocarbon absorbate layer, as previously observed from MeV He^+ irradiated Cu surfaces exposed to the ambient atmosphere[29].

NanoSIMS analysis of the enriched volume following the solid phase epitaxial (SPE) regrowth of the implanted volume of sample 3 is shown in Fig. 2e, where the ^{12}C and ^{16}O NanoSIMS depth profiles taken from both within the enriched volume as well as the unimplanted surrounding ^{Nat}Si are observed to be comparable. Concentration values were determined by assuming the upper limit for the original wafer background C and O concentration of 2.5×10^{15} cm^{-3} provided by the wafer supplier. The slight increase in the sample O signal near the surface is attributed to surface contaminants. UV Raman spectra shown in Supplementary Fig. 4, also confirm the SPE regrowth of the enriched volume after annealing. The C signal taken from the sample also shows evidence of gettering at the approximate depth of the original amorphous-crystalline interface as a result of the epitaxial regrowth process (for additional NanoSIMS carbon analysis see Supplementary Figs. 5 and 6). The minimum concentrations of ^{29}Si and ^{30}Si within the enriched volumes of samples 1–3 are shown in Table 1, where the enrichment level for all three samples is shown to be comparable (The silicon isotopic ratio NanoSIMS depth profiles from sample 3 are shown in Supplementary Fig. 7).

Structural characterisation

Transmission electron microscopy (TEM) analysis was carried out on the as-implanted enriched volume within sample 4 in order to determine the thickness of the amorphous volume above the single crystal substrate prior to annealing. Figure 3 shows the cross-sectional TEM images and corresponding fast Fourier transforms (FFTs) taken from sample 4. From the high-angle annular dark-field scanning TEM (HAADF STEM) image shown in Fig. 3a, the amorphous volume is observed to be ~250 nm deep which is comparable to the NanoSIMS depletion profile of sample 2 (Fig. 2) which shows a ~ 270 nm deep enriched volume, where a fluence variation accounts for the slight discrepancy between these samples. The diffuse rings present in the FFT taken from the high-resolution TEM image (HRTEM) shown in Fig. 3c shows the amorphous nature of the implanted volume.

Following the enrichment irradiation, a SPE anneal regrows the amorphous volume to a single crystal from the substrate. The crystalline phase of the sub-surface enriched volume of sample 5 after annealing was determined through subsequent TEM analysis, shown in Fig. 4. The bright field scanning TEM image shown in Fig. 4a shows that the enriched volume is free of defects except for a clearly defined defect layer situated ~ 225 nm from the surface. These defects are formed below the amorphous-crystalline interface upon annealing the amorphous volume[30,31], whereby the interstitial abundant region below the interface leads to the formation of extrinsic dislocation loops. The HRTEM image taken from this defect layer in Fig. 4d shows such a dislocation loop. The near-surface HRTEM image and corresponding FFT shown in Fig. 4b show that the near-surface region is single crystal, demonstrating the SPE regrowth of the amorphous volume up to the surface. For most silicon-based donor or dot architectures the qubits are located in the top ~20 nm of the substrate, which is far above the buried residual defects. For example, the flip-flop donor qubit architecture employs ^{31}P donors implanted ~15 nm below a thin surface oxide[27].

Conclusions

We have demonstrated the use of a focused beam of $^{28}Si^{++}$ ions to produce highly isotopically enriched volumes embedded in the surface of natural silicon substrates. NanoSIMS analysis has shown an isotopically enriched volume produced with a nominal $^{28}Si^{++}$ fluence of $(1.18 \pm 0.04) \times 10^{19}$ ions cm^{-2} extending over 200 nm in depth from the surface, with a residual ^{29}Si level at a minimum of 2.3 ppm. Further NanoSIMS analysis on an annealed single crystalline enriched sample shows no measurable introduction of additional impurities (e.g. C and O) into the annealed enriched volume. TEM analysis verifies the amorphous nature of the as-implanted volume as well as the single crystalline SPE regrowth upon annealing. For this highly enriched material, theoretical calculations predict Hahn-echo electron coherence times (T_{2e}^{Hahn}) exceeding 10 s[13] in the single donor regime which would be an improvement of greater than four orders of magnitude relative to the current record of 0.95 ms[6]. The advantages of the readily available FIB method are both high ^{28}Si enrichment and high elemental purity in volumes integrated within ^{Nat}Si substrates. The next step is to integrate donor-doped FIB enriched material into a device for measurement of the donor electron dephasing lifetime and hence the influence of the residual ^{29}Si atoms and lattice defects from the SPE regrowth. The silicon LMAIS eutectic alloys also provide the opportunity, without breaking vacuum, to implant the heavy group-V donor ^{123}Sb ($I = 7/2$) from AuSiSb or the optically active telecommunication band emitter ^{167}Er ($I = 7/2$) from AuSiEr. This shows the

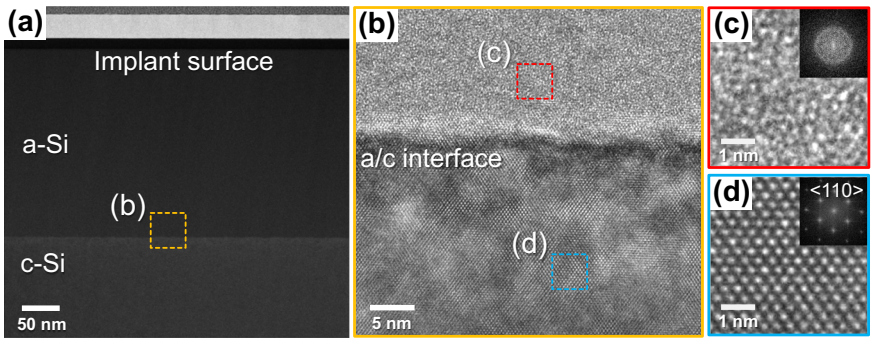

Fig. 3 | Cross-sectional TEM images of the as-implanted sample 4. a shows a HAADF STEM cross-sectional image of the sample, with the the amorphous silicon (a-Si) implanted volume and the original crystalline silicon (c-Si) below. The amorphous-crystalline (a/c) interface is shown to be very sharp and ~250 nm below the surface. **b** shows a high-resolution cross-sectional TEM image along the amorphous-crystalline interface. **c** and **d** show the HRTEM images taken from within the amorphous (enriched) region (red area in (**b**)) and the crystalline substrate beneath (blue area in (**b**)), respectively. The associated FFT taken from each image is shown in the inset. The rings observed in the FFT of part (**c**) taken above the interface indicate that the implanted volume is amorphous as compared to the single crystalline substrate beneath.

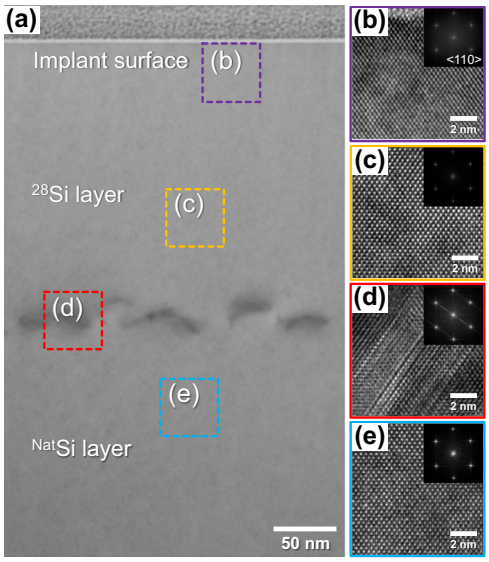

Fig. 4 | Cross-sectional TEM images of sample 5 post-anneal. a shows the bright field (BF) STEM cross-sectional image of the annealed sample. The enriched volume is shown to be free of any defects barring a narrow layer found ~ 225 nm below the surface. A series of HRTEM images taken of areas across the sample corresponding to different distances from the implanted surface (as denoted by the coloured boxes in (**a**)) are shown in (**b**–**e**) where the associated FFT taken from each image is shown in the inset. The similarity of the FFTs taken from the near-surface region (**b**) and the single crystalline substrate beneath the implanted volume (**e**) verifies the complete single crystalline regrowth of the enriched volume. **d** shows the presence of an extrinsic dislocation loop within the defect layer.

potential of the FIB enrichment method to produce enriched and doped silicon for novel quantum device architectures.

Methods

Sample fabrication

The un-implanted sample substrate was an undoped > 10 kΩ·cm [100] 500 μm ^{Nat}Si wafer. The background levels of carbon and oxygen were both quoted by the supplier (University Wafer, Inc.) as having an upper limit of 2.5×10^{15} cm^{-3}. All samples were cleaned and then dipped in hydroflouric acid (HF) prior to loading into the P-NAME sample vacuum chamber in order to remove the native silicon oxide. The ion beam current was measured using a Faraday cup on the sample stage which was connected to a Keithley 6285 picoammeter. The nominal ion beam profile on the sample was assumed to be a Gaussian point spread function where 2σ was taken as the ion beam width. The ion beam width was measured using the 20/80 knife-edge method from a line-scan taken over a sharp high-contrast metal edge using the secondary electron signal. The signal intensity as a function of the beam position in the line scan was fitted with an error function using the GaussFit plugin (based on the ASTM E986-9731) within the ImageJ software package and the 20–80% amplitude was taken as the ion beam width. Following irradiation some samples were annealed in an ambient Ar atmosphere using an Annealsys model AS-One 100 rapid thermal annealer (RTA) (RTA SPE regrowth annealing recipe temperature profile shown in Supplementary Fig. 8).

Atomic force microscopy

AFM measurements for sample 3 were carried out using a Nanosurf coreAFM 190Al-G tip which was operated in tapping mode. AFM measurements for samples 1 and 2 were taken using a neaSNOM scattering-type near-field optical microscope operated in tapping-mode using a Pt-coated, grounded AFM tip. For all the samples the raw AFM image height correction was carried out using the Gwyddion software package (version 2.62) to measure the swelling of the implanted volume.

NanoSIMS analysis

A CAMECA NanoSIMS 50L instrument employing a 16 keV Cs^+ beam with a beam current of 0.43–0.48 pA was used to sputter the target sample in turn generating negative secondary ions from the surface. A double-focusing mass spectrometer was employed to detect the ions produced. The instrument is equipped with seven detectors that each register a specific pre-defined ion species. For both samples 2 and 3 the detector configuration was $^{12}C^-$, $^{16}O^-$,$(^{12}C^{14}N)^-$, $^{28}Si^-$, $^{29}Si^-$, $^{30}Si^-$, $^{16}O_2^-$ whereas for sample 1 the configuration was $^{12}C^-$, $^{28}Si^-$, $^{29}Si^-$, $^{30}Si^-$, $^{16}O_2^-$, $^{12}C_3^-$. The mass resolution of the instrument was set to be greater than 6000 $M/\Delta M$ so that the ^{29}Si could be separated from the ^{28}SiH mass interference and the ^{30}Si from the ^{29}SiH. 5 μm by 5 μm raster scans were taken from within the centre of each of the enriched volumes except for sample 3 where a series of raster scans were taken from different areas across the enriched volume. Each scan was composed of 256 by 256 pixels leading to a pixel resolution of 19.5 nm per pixel with a dwell time set to 2 ms per pixel. Slit positions, designated D1-4 (150 μm in diameter), ES-3 (30 μm width) and AS-2 (200 μm width) were utilised. The instrument analysis chamber was held at a vacuum of the order of 10^{-10} mbar. All samples analysed using the tool were HF dipped prior to loading into the SIMS machine chamber. NanoSIMS data were processed using either the Open MIMS image plugin found in the ImageJ software package or the L'image software package developed by L. Nittler at the Carnegie Institution of Washington. AFM measurements of the sputtered SIMS craters were taken to calibrate the depth of the isotope profiles after the SIMS analysis assuming a constant sputtering rate.

TEM analysis

TEM analysis was carried out on both samples 4 and 5 in order to verify the amorphous implanted volume depth and the regrowth quality of the enriched volume upon annealing, respectively. Cross-sectional lamella taken from both samples were prepared by FIB milling using an FEI Helios 660 FIB. Prior to lamella FIB extraction both samples were ex situ coated with a thin carbon layer followed by a AuPd layer to mitigate charging effects and to protect the surface from FIB damage. A further ~300 nm thick sacrificial Pt layer was then deposited via electron beam to protect the film from any Ga ion implantation during the milling process. This was followed by a final ~3 μm thick Pt protective layer that was deposited using the Ga ion beam. Cross-sectional TEM and HAADF images were taken of both samples using a Talos F200X S/TEM tool operating at 200 keV. The TEM image shown in Fig. 4a was filtered in order to reduce the visibility of surface damage and redeposited Pt contamination introduced during the lamellae sample preparation (raw data in Supplementary Fig. 9).

Data availability

The data that support the findings of this study are available from R.J.C. upon reasonable request.

Received: 18 October 2023; Accepted: 5 April 2024;
Published online: 07 May 2024

References

1. Lock, E. H. et al. Materials innovations for quantum technology acceleration: a perspective. *Adv. Mater.* **35**, 2201064 (2023).
2. Takeda, K., Noiri, A., Nakajima, T., Kobayashi, T. & Tarucha, S. Quantum error correction with silicon spin qubits. *Nature* **608**, 682–686 (2022).
3. Saraiva, A. et al. Materials for silicon quantum dots and their impact on electron spin qubits. *Adv. Funct. Mater.* **32**, 2105488 (2022).
4. Kane, B. E. A silicon-based nuclear spin quantum computer. *Nature* **393**, 133–137 (1998).
5. Chatterjee, A. et al. Semiconductor qubits in practice. *Nat. Rev. Phys.* **3**, 157–177 (2021).
6. Muhonen, J. T. et al. Storing quantum information for 30 seconds in a nanoelectronic device. *Nat. Nanotechnol.* **9**, 986–991 (2014).

7. Dehollain, J. P. et al. Optimization of a solid-state electron spin qubit using gate set tomography. *N. J. Phys.* **18**, 103018 (2016).
8. Khoury, M. & Abbarchi, M. A bright future for silicon in quantum technologies. *J. Appl. Phys.* **131**, 200901 (2022).
9. Abe, E. et al. Electron spin coherence of phosphorus donors in silicon: effect of environmental nuclei. *Phys. Rev. B* **82**, 121201 (2010).
10. Rosman, K. J. R. & Taylor, P. D. P. Isotopic compositions of the elements 1997. *J. Phys. Chem. Ref. Data* **27**, 1275–1287 (1998).
11. de Sousa, R. & Das Sarma, S. Theory of nuclear-induced spectral diffusion: spin decoherence of phosphorus donors in Si and GaAs quantum dots. *Phys. Rev. B* **68**, 115322 (2003).
12. Witzel, W. M. & Das Sarma, S. Quantum theory for electron spin decoherence induced by nuclear spin dynamics in semiconductor quantum computer architectures: Spectral diffusion of localized electron spins in the nuclear solid-state environment. *Phys. Rev. B* **74**, 035322 (2006).
13. Witzel, W. M., Carroll, M. S., Morello, A., Cywiński, Ł. & Das Sarma, S. Electron spin decoherence in isotope-enriched silicon. *Phys. Rev. Lett.* **105**, 187602 (2010).
14. Itoh, K. M. & Watanabe, H. Isotope engineering of silicon and diamond for quantum computing and sensing applications. *MRS Commun.* **4**, 143–157 (2014).
15. Becker, P., Pohl, H.-J., Riemann, H. & Abrosimov, N. Enrichment of silicon for a better kilogram. *Phys. Status Solidi (a)* **207**, 49–66 (2010).
16. Abrosimov, N. V. et al. A new generation of 99.999% enriched ^{28}Si single crystals for the determination of avogadro's constant. *Metrologia* **54**, 599 (2017).
17. Dwyer, K. J., Pomeroy, J. M., Simons, D. S., Steffens, K. L. & Lau, J. W. Enriching ^{28}Si beyond 99.9998% for semiconductor quantum computing. *J. Phys. D Appl. Phys.* **47**, 345105 (2014).
18. Tang, K., Kim, H. S., Ramanayaka, A. N. R., Simons, D. S. & Pomeroy, J. M. A compact, ultra-high vacuum ion source for isotopically enriching and depositing ^{28}Si thin films. *Rev. Sci. Instrum.* **90**, 083308 (2019).
19. Tang, K., Kim, H. S., Ramanayaka, A. N., Simons, D. S. & Pomeroy, J. M. Targeted enrichment of ^{28}Si thin films for quantum computing. *J. Phys. Commun.* **4**, 035006 (2020).
20. Holmes, D. et al. Isotopic enrichment of silicon by high fluence $^{28}Si^{-}$ ion implantation. *Phys. Rev. Mater.* **5**, 014601 (2021).
21. Vandersypen, L. M. K. et al. Interfacing spin qubits in quantum dots and donors—hot, dense, and coherent. *npj Quantum Inf.* **3**, 34 (2017).
22. Savytskyy, R. et al. An electrically driven single-atom "flip-flop" qubit. *Sci. Adv.* **9**, eadd9408 (2023).
23. Mądzik, M. T. et al. Controllable freezing of the nuclear spin bath in a single-atom spin qubit. *Sci. Adv.* **6**, eaba3442 (2020).
24. Adshead, M. et al. A high-resolution versatile focused ion implantation platform for nanoscale engineering. *Adv. Eng. Mater.* **25**, 2300889 (2023).
25. Möller, W. & Eckstein, W. Tridyn—a trim simulation code including dynamic composition changes. *Nucl. Instrum. Methods Phys. Res. Sect. B: Beam Interact. Mater. At.* **2**, 814–818 (1984).
26. Möller, W., Eckstein, W. & Biersack, J. P. Tridyn-binary collision simulation of atomic collisions and dynamic composition changes in solids. *Comput. Phys. Commun.* **51**, 355–368 (1988).
27. Tosi, G. et al. Silicon quantum processor with robust long-distance qubit couplings. *Nat. Commun.* **8**, 450 (2017).
28. Aboura, Y. & Moore, K. L. Nanosims analysis of hydrogen and deuterium in metallic alloys: artefacts and best practice. *Appl. Surf. Sci.* **557**, 149736 (2021).
29. Kellock, A. J. et al. Mechanism for ion beam passivation of copper surfaces. *Nucl. Instrum. Methods Phys. Res. Sect. B Beam Interact. Mater. At.* **127-128**, 742–746 (1997).
30. Bonafos, C., Mathiot, D. & Claverie, A. Ostwald ripening of end-of-range defects in silicon. *J. Appl. Phys.* **83**, 3008–3017 (1998).
31. Jones, K. S., Prussin, S. & Weber, E. R. A systematic analysis of defects in ion-implanted silicon. *Appl. Phys. A* **45**, 1–34 (1988).
32. Mazzocchi, V. et al. 99.992 % ^{28}Si CVD-grown epilayer on 300 mm substrates for large-scale integration of silicon spin qubits. *J. Cryst. Growth* **509**, 1–7 (2019).
33. Sabbagh, D. et al. Quantum transport properties of industrial $^{28}Si/^{28}SiO_2$. *Phys. Rev. Appl.* **12**, 014013 (2019).
34. Li, J.-Y., Huang, C.-T., Rokhinson, L. P. & Sturm, J. C. Extremely high electron mobility in isotopically-enriched ^{28}Si two-dimensional electron gases grown by chemical vapor deposition. *Appl. Phys. Lett.* **103**, 162105 (2013).

Acknowledgements

This work was funded by the Australian Research Council Discovery Project DP220103467 and the University of Melbourne/ University of Manchester collaboration scheme. D.N.J. acknowledges the support of a Royal Society (UK) Wolfson Visiting Fellowship RSWVF/211016. R.A. acknowledges the support of a Melbourne Research Scholarship. This work was funded by the EPSRC grants EP/R025576/1, EP/V001914/1 and EP/R00661X/1 (Henry Royce Institute) and by capital investment by the University of Manchester. S.J.H. acknowledges the European Research Council under the European Union's Horizon 2020 research and innovation programme (grant agreement No. 715502, EvoluTEM). Electron microscopy access was supported by the Henry Royce Institute for Advanced Materials, funded through EPSRC grants EP/S019367/1, EP/P025021/1 and EP/P025498/1. The NanoSIMS was funded by UK Research Partnership Investment Funding (UKRPIF) Manchester RPIF Round 2 and also supported by the Henry Royce Institute for Advanced Materials. B.G. and J.L.B. thank EPSRC for support through grants EP/T01914X/1, EP/S037438/1 and capital investment via University of Manchester and Royce Institute. J.L.B. also acknowledges funding from UKRI via MR/T022140/1. The authors acknowledge useful discussions with J.C. McCallum, A.M. Jakob, S.Q. Lim and A. Morello.

Author contributions

R.A. led the isotopic enrichment implantation experiments with assistance from M.C. and M.A. under the supervision of D.N.J. and R.J.C. NanoSIMS analysis was carried out by K.L. under the supervision of K.L.M. TEM analysis was carried out by R.C. and B.A. under the supervision of S.J.H. J.J. assisted with pre- and post-implantation processing. Raman measurements were conducted by M.A. and J.J. AFM measurements were carried out by M.C. and A.B.G. under the supervision of J.L.B. Data were analysed by R.A., D.N.J. and R.J.C. R.A, R.J.C. and D.N.J. wrote the manuscript with input from all other authors.

Competing interests

The authors declare no competing interests.

Additional information

Supplementary information The online version contains supplementary material available at https://doi.org/10.1038/s43246-024-00498-0.

Correspondence and requests for materials should be addressed to Ravi Acharya or Richard J. Curry.

Peer review information *Communications Materials* thanks Takashi Kobayashi, Francesco Biccari and the other, anonymous, reviewer(s) for their contribution to the peer review of this work. Primary Handling Editor: Aldo Isidori. A peer review file is available.

Reprints and permissions information is available at http://www.nature.com/reprints

Publisher's note Springer Nature remains neutral with regard to jurisdictional claims in published maps and institutional affiliations.

Open Access This article is licensed under a Creative Commons Attribution 4.0 International License, which permits use, sharing, adaptation, distribution and reproduction in any medium or format, as long as you give appropriate credit to the original author(s) and the source, provide a link to the Creative Commons licence, and indicate if changes were made. The images or other third party material in this article are included in the article's Creative Commons licence, unless indicated otherwise in a credit line to the material. If material is not included in the article's Creative Commons licence and your intended use is not permitted by statutory regulation or exceeds the permitted use, you will need to obtain permission directly from the copyright holder. To view a copy of this licence, visit http://creativecommons.org/licenses/by/4.0/.

© The Author(s) 2024